

Full Length Article

Ostwald ripening microkinetic simulation of Au clusters on MgO(001)

Samantha Francis^a, Alexandre Boucher^a, Glenn Jones^b, Alberto Roldan^{a,*}^a Cardiff Catalysis Institute, School of Chemistry, Cardiff University, Main Building, Park Place, Cardiff, CF10 3AT, Wales, United Kingdom^b Johnson Matthey Technology Center, Blounts Ct Rd, Sonning Common, Reading RG4 9NH, United Kingdom

ARTICLE INFO

Keywords:

Sintering
Ostwald ripening
DFT
Supported catalyst
Microkinetics
Bottom-up approach

ABSTRACT

Sintering is one of the most common processes responsible for the loss of supported metal nanoparticle catalysts' activity. We have combined ab-initio calculations with microkinetic simulations to investigate the digestion and growth mechanism on Au clusters supported on MgO(001) following a bottom-up approach. The energy barrier for diffusing a single gold atom on the clean MgO surface was found to be 0.29 eV in full agreement with previous reports. Additionally, and as an extension to the entire energy profile related to Ostwald mechanisms, we found all of the activation energies to be below 1.05 eV in the cases investigated. An odd-even cluster trend was observed during ripening, attributed to the stability of pairing the unpaired electrons associated with the single gold atoms. Microkinetic analyses showed that Au single atoms are present on the surface of magnesia up to a temperature of 160 K. At higher temperatures, the system has enough energy for the single atom to diffuse across the surface and attach to other atoms or clusters. At temperatures akin to room temperature, the cluster undergoes ripening to form larger particles in order to achieve a more stable equilibrium.

1. Introduction

Heterogeneous catalysts provide an alternative, more favourable, reaction pathway for many chemical industry processes such as manufacturing and energy conversion.[1] The efficacy of these catalysts is determined by their composition, size, shape and resilience of the active sites under reaction conditions.[2–6] Commonly built by late transition metal nanoparticles (NPs), the desired active phase of the catalyst is dependent on the application in question. Nevertheless, catalysts must generally possess a large area of active sites and be highly resilient towards changing conditions and the presence of pollutants.

Many processes can lead to catalyst deactivation, including poisoning, phase changes and mechanical straining, in addition to sintering.[7] Poisoning occurs when species are irrevocably adsorbed onto the catalyst surface, preventing other species from adsorbing to undergo surface reactions. A step further from poisoning is a phase change, where the adsorbate is incorporated into the lattice structure. Mechanical strain can also cause changes in the active sites' shapes and size through attrition, which can commonly occur from temperature fluctuations in the catalyst preparation and during the reaction. As mentioned, one of the most common processes that affect NP's size and shape is sintering. This process has been shown to have a dramatic effect on catalytic activity[8] as it influences the number of active sites and their electronic

structure.[9] Sintering is driven by reducing the surface-bulk ratio[10] and can be exacerbated by heat treatment during catalyst synthesis methods and reaction conditions.[11–14] Two principal mechanisms have been established to contribute to the enlargement of NPs: coalescence and Ostwald ripening.[15] During coalescence,[16] a whole cluster will migrate, collide with another particle and merge to form a single larger nanoparticle, also known as Smoluchowski ripening. During Ostwald ripening, a single atom breaks off (digests) from the less stable moiety (Ostwald digestion) and diffuses randomly across the surface until interacting with another cluster, where it is enveloped onto the new, more stable structure.[17] The sintering process is challenging to reverse, and the cost of replacing inactive catalysts can be very high not only from an engineering perspective, but also due to the cost of the expensive metals generally involved in catalysis. Through a better understanding of sintering rates and its mechanisms, deactivating processes can be minimized or possibly reversed by redispersion of the metal on the catalyst surface.[18]

Nanosize gold has been investigated for its catalytic properties since discovering the reactivity of Au NPs for reactions such as oxidation of CO at low temperatures,[19] acetylene hydrochlorination,[20] alcohol oxidation,[21] and activation of molecular oxygen.[22] These significant findings have prompted a flurry of research into understanding the activity of supported gold catalysts and the discovery of new uses.

* Corresponding author.

E-mail address: roldanmartineza@cardiff.ac.uk (A. Roldan).<https://doi.org/10.1016/j.apsusc.2021.151317>

Received 7 June 2021; Received in revised form 11 August 2021; Accepted 14 September 2021

Available online 25 September 2021

0169-4332/© 2021 The Author(s). Published by Elsevier B.V. This is an open access article under the CC BY license (<http://creativecommons.org/licenses/by/4.0/>).

Correspondingly, magnesium oxide (MgO) has been used extensively as support material for metal catalysts,[23–25] in surface science[26] and electronics.[27,28] MgO is a prototypical example of a non-reducible metal oxide support, which crystallizes in a simple rock salt structure [29,30] exposing, relatively defect-free, its most stable surface, MgO (001).[31,32] This size-dependent activity of Au/MgO(001) systems has been comprehensively discussed previously, and has been attributed to the properties that NPs exhibit,[33] i.e. a high surface-to-bulk ratio, the availability of low-coordination atoms,[34] and the presence of perimeter sites at the Au – support interface.[35] Additionally, common supported metal catalysts' properties, and Au/MgO is not an exception, are also influenced by the substrate-induced strain at the interface and the epitaxial stress within the cluster itself.[36] In a study measuring the magnitude of moiré fringes on a range of clusters supported on MgO, the authors found that Au clusters change morphology to become 3D clusters at Au weight loadings above 1.5 wt%.[37]

Previous microkinetic models built by Campbell *et al.*[12,13] rationalized Oswald's ripening of supported Au NPs on TiO₂ using a relation between the coverage of TiO₂'s surface as a function of the temperature, providing the NPs' growth speed as a function of time. Using experimental data in such model with a heating rate of 1 K s⁻¹, they found results in a good agreement with experimental measurement of the Au covering on a TiO₂ surface. This method can be seen as a 'top-down' approach, starting from macroscopic observations such as surface coverage and approximated particles' mean average radius. We developed a bottom-up approach in the present work and applied it to the ripening and digestion of Au_n/MgO clusters (n < 10 atoms). We combined electronic structure analysis and microkinetic simulations to rationalize the cluster size distribution as a function of the temperature and Au loading.

2. Computational details

Supported Au clusters of up to 10 atoms in size were modelled using spin-polarized periodic plane-wave density functional theory (DFT) calculations performed within the Vienna Ab Initio Simulation Package (VASP).[38–40] The PBE density functional of Perdew, Burke, and Ernzerhoff[41] was used to calculate the exchange and correlation contributions and projector-augmented wave (PAW) pseudopotentials to describe the core electrons.[40,42] Dispersion interactions were computed using Grimme's empirical dispersion correction DFT-D3.[43] The plane-wave kinetic cut-off was set at 450 eV, and a 3 × 3 × 1 Monkhorst-Pack k-point grid was used after benchmarking the Brillouin zone. Dipole corrections were applied perpendicular to the surfaces upon Au adsorption.

A MgO slab model of the most stable (001) surface was created from the optimized bulk structure, with lattice parameter 4.195 Å. Considering the computational time and the strength of the lateral interactions between periodically repeated Au clusters, we considered a slab with a surface area of 281.6 Å² built with a thickness of two-layer consisting of 64 magnesium and 64 oxygen where the bottom layer was fixed. The slabs were separated by 20 Å vacuum fitted in the z-direction. This slab model's accuracy was measured by appropriate benchmarking, see reference 44.

We calculated the adhesion energy (E_{adh}) using Eq. (1) to measure the interaction's strength between the cluster and the surface. The clusters' morphology in the gas phase (Au_n) is the same as the optimized cluster on the support (Au_n/Surf), and therefore, E_{adh} does not include any deformation energies, i.e., the adsorption energy is referred to gas-phase clusters at the same geometry as supported.

$$E_{adh} = \frac{E_{Au_n/Surf} - (E_{Surf} + E_{Au_n})}{n} \quad (1)$$

In the Eq. (1) above, E_{Surf} indicates the energy of a naked MgO(001) surface. We also calculated the binding energy per cluster atom (E_b) using Eq. (2) and an isolated single gold atom (E_{Au1}).

$$E_b = \frac{E_{Au_n/Surf} - (E_{Surf} + n \cdot E_{Au1})}{n} \quad (2)$$

The clusters' cohesion energy (E_{coh}) provides a measure of the interaction strength between atoms in the cluster and is calculated using the following Eq. (3):

$$E_{coh} = \frac{E_{Au_n} - n \cdot E_{Au1}}{n} = \frac{E_b - E_{adh}}{n} \quad (3)$$

The energy barriers across the energy profile were determined by locating the transition states for atomic diffusion and attachment. A static path extrapolation technique was initially used to search for transition states along the reaction pathways, followed by a complete quasi-newton optimization of the identified transition state (TS). Frequency calculations were used to characterize the minima and transition states, based on the absence or presence of a single imaginary mode respectively.

2.1. Au structures

We used an unbiased genetic algorithm to search low energy structures of small Au_n clusters (n ≤ 5 atoms) and build larger moieties exploring an extensive range of structures.[44] Single-atom attachment and diffusion activation energies (E_a) were calculated with Eq. (4) to understand ripening processes:

$$E_a = E_{TS} - E_{Au_{n+1}} \quad (4)$$

Where the $E_{Au_{n+1}}$ is the energy of the system with both, the Au_n cluster and the single atom on the same slab before attachment, and the E_{TS} is the energy at the transition state along the attachment reaction coordinates.

2.2. Microkinetic methodology

We employed microkinetic modelling to extrapolate DFT results within a transition state theory (TST) framework, including the mean-field effect of temperature and Au coverage (θ).[45] TST limitations include a disregard for short-lived intermediates and failure at high temperatures.[46] This approach has shown to be very effective to describe reaction dynamics and rates from a bottom-up perspective. The methodology here employed is detailed elsewhere.[45,47–50] Applied to Ostwald coalescence processes, the elementary steps are diffusion, attachment and detachment of single atoms. The constant rate (k) of each elementary surface step is commonly computed using the following equation of Eyring, Evans and Polanyi:[51]

$$k = A e^{\frac{-\Delta G}{RT}}, \quad A = \frac{K_B T}{h} \frac{Q_{TS}}{Q_R} \quad (5)$$

Where h is the Plank constant, K_B is the Boltzmann constant and T the temperature. The calculated partition function for the transition state (Q_{TS}) and the reactants (Q_R) are used to calculate the pre-exponential factor (A). The entropic and the enthalpic contribution to the Gibbs free energy equation are derived from the partition functions. The reaction activation energy (ΔG) is calculated from the Gibbs free energies of the TS and the reactants.

As part of the discussion regarding the microkinetic simulations, the metal dispersion was also calculated. In the first microkinetic experiment, we considered one atom per simulation cell leading to 3.552 × 10¹⁷ Au atoms per m², equivalent to 1.16 × 10⁴ g_{Au} m⁻², and a metal dispersion of 8608.44 m² g_{Au}⁻¹.

3. Results and discussion

The data collected in Table 1 shows that an increase in cluster size

Table 1

Summary of the adsorption (E_{adh}), cohesion (E_{coh}), binding (E_b) energies, magnetization (M_s) and charge ($q(\text{Au}_n)$) of the lowest energy configurations obtained for the Au_n/MgO ($n \leq 10$) system. The cluster spin magnetization shows a distinct odd-even trend associated with the accommodation of the unpaired electron of Au atom.

n	E_{adh} (eV/atom)	E_{coh} (eV/atom)	E_b (eV/atom)	M_s (μ_B)	Average $q(\text{Au}_n)$ (e)
1	1.37	0.00	1.37	1.00	0.24
2	1.00	1.15	2.15	0.00	0.12
3	0.93	1.20	2.13	0.97	0.11
4	0.86	1.50	2.36	0.00	0.12
5	0.66	1.67	2.33	0.89	0.11
6	0.65	1.89	2.54	0.00	0.10
7	0.66	1.86	2.51	0.54	0.10
8	0.66	1.99	2.65	0.00	0.10
9	0.64	1.98	2.62	0.24	0.10
10	0.60	2.08	2.68	0.00	0.08

increases cohesion energy (E_{coh}) and decreases adhesion energy (E_{adh}) per cluster atom. Cluster structures are included in Table S1 in the [supplementary Information](#) and detailed in reference 44. The overall interaction is expressed by the binding energy (E_b), overall showing an increase in the $\text{Au}_n/\text{MgO}(001)$ stability with increasing the clusters' size (n). This finding is in line with the accepted idea that particle size will increase to minimize the surface-bulk ratio.[52] Along with the decrease in adsorption energy and the increase in binding energy, the Bader charge analyses show that the charge transfer from the surface to the Au atoms decreases with the cluster size, remaining close to 0.1 e per Au atom (Table 1). Such charge transfer implies that while the association between Au atoms is favoured, the interaction with the surface becomes less critical with cluster growth. The supported odd-numbered clusters of Au atoms have an unpaired electron in the 6 s orbital, the resultant magnetization of which, decreases with cluster size as the electrons are increasingly delocalized. Clusters with an even number of atoms undergo electron pairing, to reinforce their stabilization, see Table 1, which results in an overall cluster magnetization of 0 μ_B . Therefore, during the sintering process, one should expect a change in the catalyst's total magnetization due to the disappearance of Au_1 , which could be measurable, for instance, by electron spin resonance (ESR).

3.1. Single-atom migration mechanism

Two stable positions were found for a single Au atom on $\text{MgO}(001)$, on top of an O atom and on top of an Mg atom.[44] Bridge sites are not stable, and upon optimization, the Au atom lay on top of an O atom. A hollow site was optimised using a conjugate gradient algorithm leading to minimas in the potential energy although upon analysis of its vibrational modes, we found it to be the transition state between O-top sites with an imaginary vibrational frequency of -32 cm^{-1} . The most stable of these positions, with adhesion energy of 1.37 eV is on top of an O atom, which compares to a value of 0.89 eV atop an Mg atom, in agreement with previous computational work[53] and it is also supported by experimental electron paramagnetic resonance (EPR) in combination with infrared reflection-absorption (IRAS) spectroscopic data produced by Yulikov et al.[54]

We investigated two possible diffusion pathways from one O-top position to an adjacent one: i) the path in a straight line crossing the hollow site and ii) the path across the magnesium atom. The energy barrier for the process across the hollow was measured to be 0.29 eV, while the E_a across the Mg is 0.22 eV higher.

The surface diffusion coefficient (D_s) at a temperature (T) of an entity performing a random walk within the validity of the transition state theory is given by the relation in Eq. (6):

$$D_s = D_{s0} \exp\left(-\frac{E_a}{K_B T}\right), \quad (6)$$

where D_{s0} is a frequency factor, and E_a is the activation energy controlling the diffusion pathway. For an isolated atom migrating on a surface, D_{s0} can be obtained from the Einstein relation of a random walk:[55]

$$D_{s0} = \frac{K_B T}{h} \frac{nd^2}{2\alpha} \quad (7)$$

In Eq. (7) we have neglected the entropy and the vibrational contribution to the energy, α is the dimensionality of the motion ($\alpha = 2$), d is the jump distance, and n is the number of jump directions available to the adatom on the surface of $\text{MgO}(001)$ ($n = 4$). Using zero-point energies (E_{ZPE} , in Eq. (8)) to correct the energy (E) in initial and transition leading to E_a , the diffusion coefficient (D_s , usually in cm^2s^{-1}) becomes Eq. (9), and, at 300 K, the pre-factor (D_{s0}) is calculated at $6.89 \times 10^{-4} \text{ cm}^2\text{s}^{-1}$ and the surface diffusion (D_s) is $6.29 \times 10^{-9} \text{ cm}^2\text{s}^{-1}$, which are comparable to those of self-diffusion atoms.[56] In Eq. (8), c is the speed of light in $\text{cm}\cdot\text{s}^{-1}$, in line with the vibrational frequencies (ν) units (cm^{-1}).

$$E_{ZPE} = E + \frac{1}{2} \sum_i h c \nu_i, \quad (8)$$

$$D_s = \frac{K_B T}{h} d^2 \exp\left(-\frac{\Delta E_{ZPE}}{K_B T}\right) \quad (9)$$

3.2. Ostwald ripening mechanism

We placed the migrating atom at approximately two oxygen away from the cluster, ensuring that it is on a stable position far enough to avoid any interaction with the cluster. Distances further away were investigated, which were calculated to have negligible energy differences. However, a starting distance nearer, the atomic relaxation forces the single-atom to bind the cluster. Hence, from a separated position and moving along the reaction coordinate, the coalescent atom crosses the hollow site toward the cluster and upon overcoming the E_a merges with the cluster, as illustrated in Fig. 1. We have assumed that, once the Au_1 atom combines with the cluster Au_n , the atomic rearrangement to the most stable geometry of Au_{n+1} has an energy barrier lower than the attachment and migration barriers. Energetic and structural information relating to each cluster size's ripening energies can be found in Table 2.

In general, the greater the cluster size, the greater the stability of the cluster. Additionally, the formation of an even number of atoms clusters is more favourable than odd clusters, resulting in the odd-even behaviour. The structural analysis shows that as the cluster size increases, the average surface to cluster distance ($\overline{dAu-S}$) also increases due to the larger number of atoms in contact with the surface (interface atoms) although individual Au atoms' interaction decreases. This trend is supported by the decrease in E_{adh} with the cluster size. However, there is some deviation from this trend, $\overline{dAu-S}$ increases from 2.2 Å to 2.7 Å between Au_5 and Au_6 . This increase can be associated with the point at which the clusters lie parallel ($n \geq 6$) rather than perpendicular ($n < 6$) to the surface. When the clusters lie flat, parallel to the surface, the number of atoms at the interface increases suddenly and $\overline{dAu-S}$ increases as the interaction of individual atoms with the surface decreases more rapidly than in perpendicular arrangements. Au_8 does not follow this trend due to its unique geometric feature, shown in Fig. 2, which displays the square symmetry (001)-like configuration in the centre, rather than the typical (111) arrangement seen for all other clusters at this scale.[44] The Au_8 configuration creates slightly shorter bonds between the Au atoms in the (001) arrangement and results in a lower $\overline{dAu-S}$.

Generally, the activation barriers associated with single-atom attachment in all systems is relatively small ($< 1.05 \text{ eV}$ from Table 2). This trend can be explained by the reasonably high mobility of gold atoms on the MgO support[57] and the lack of defects or adsorbed

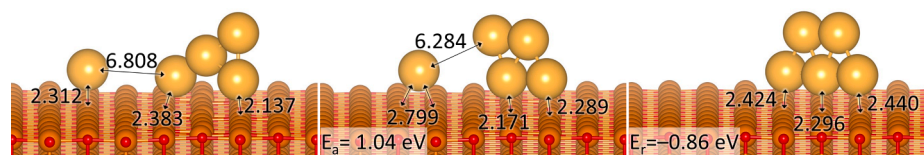


Fig. 1. Representation of a single atom attachment path to an Au_4 cluster leading to Au_5 . Distances are represented in Angstroms between Au and the binding oxygen. The colour scheme is as follows: Orange = Mg, red = O and gold = Au.

Table 2

Summary of ripening barriers (E_a) and attachment reaction energies (E_r), the average surface to cluster distances ($\overline{dAu-S}$) and the average cluster Au-Au distances ($\overline{dAu-Au}$).

(Au_n)	(Au_{n+1})	E_a /eV	E_r /eV	$\overline{dAu-S}$ (Å)	$\overline{dAu-Au}$ (Å)
1	2	0.73	-0.93	2.198	2.516
2	3	0.31	-0.77	2.292	2.596
3	4	0.25	-1.76	2.207	2.654
4	5	1.04	-0.86	2.239	2.712
5	6	0.14	-2.34	2.705	2.716
6	7	0.34	-1.05	2.695	2.740
7	8	0.21	-2.21	2.676	2.710
8	9	0.68	-1.06	2.710	2.793
9	10	0.23	-1.90	2.731	2.746

species stabilizing specific moieties.[58,59] The formation of an even number cluster is associated with considerable reaction energy (E_r) compared to an odd-numbered cluster. Once formed, odd number clusters have an unpaired electron rendering the single atom's attachment less favourable, whereas the electrons are paired for the even-number cluster sizes. This pairing interaction is evidenced by the cluster magnetization described in Table 1, Figs. 3 and 4. Fig. 4 highlights that odd-numbered clusters will react exothermically with Au_1 to pair its electrons forming an even-numbered cluster of superior stability. Note the lack of magnetisation in even-numbered clusters in Table 1, whereas the same system with a neighboring Au_1 will present an unpaired electron (Fig. 3). The formation of an odd numbered cluster presents the opposite trends as shown by clearly by the Au_4 growth, which has the largest E_a

not only because of intaking an unpaired electron but also because it marks the transition towards moieties parallel to the surface by weakening the interphase interaction and substantially increasing its $\overline{dAu-S}$ from 2.239 Å in Au_4 to 2.705 Å in Au_5 (see Table 2).

Fig. 5 illustrates the trend between activation (E_a) and reaction (E_r) energies of the ripening process, which appears to follow the Brønsted-Evans-Polanyi (BEP) principle; $R^2 = 0.9$ – excluding the particular cases of Au_2 , Au_4 and Au_6 . These three clusters have all the electrons paired and, while the activation energy to for the process $Au_{n+1} \rightarrow Au_5$ highlights the Au_4 stability, the low E_a on Au_{2+1} and Au_{6+1} represents the instability of Au_2 and Au_6 . Indeed, Au_2 sits perpendicular to the surface with a very low coordination, which is proportional to the surface energy. The transition state to form Au_3 is at 5.9 Å from Au_2 , which points to a dissimilar initial state compared with the other processes. Similar out-of-trend behaviour is found on $Au_{6+1} \rightarrow Au_7$ where the Au_6 mismatch with the support strains the $Au-Au$ bonds, as seen on the $\overline{dAu-Au}$ in Table 2, promoting its growth. The BEP principle is widely used to estimate a vast number of molecular systems' reactivity, but has not been considered in ripening mechanisms before. Further detail on such analysis would accelerate investigations on larger clusters and nanoparticles.

3.3. Ripening simulations

We have integrated the energetic information presented above into microkinetic models to simulate two processes: cluster ripening and cluster digestion. The microkinetic model's application shows the distribution of the species in the system at a specific temperature (T) and time (t) with varying initial Au dispersions. The temperature increases to

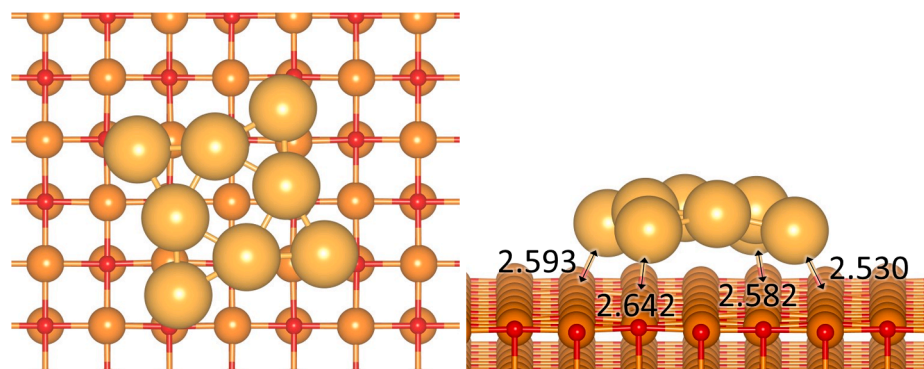


Fig. 2. Schematic representation of the most stable geometry of $Au_8/MgO(001)$. Distances are in Angstroms between Au atoms and binding oxygen. The colour scheme is orange = Mg, red = O and gold = Au.

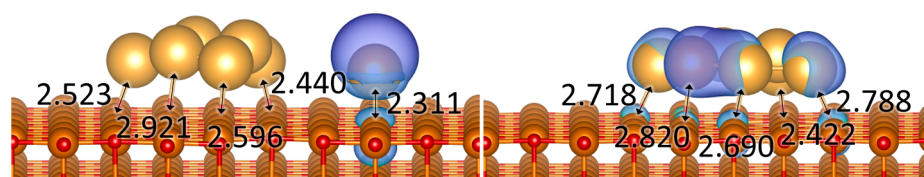


Fig. 3. Representation of $Au_6 + 1$ and Au_7 cluster systems showing (left) the magnetization located entirely on Au_1 , and (right) the magnetization delocalized over Au_7 . Distances are in Angstroms between Au atoms and binding oxygen, and isosurface level is $0.001 \text{ e}/\text{Å}^3$. Colour scheme is orange = Mg, red = O and gold = Au.

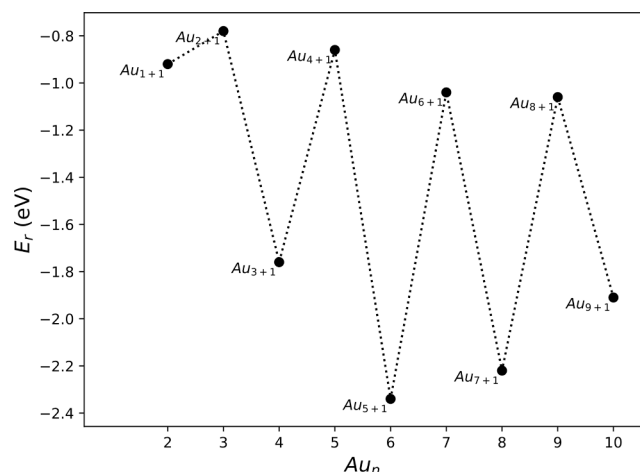


Fig. 4. Summary of the reaction energies (E_r) associated with the Au_n cluster's formation and growth.

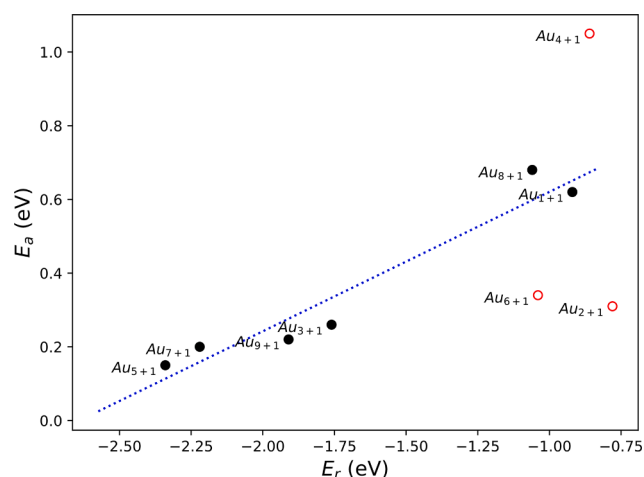


Fig. 5. Activation energy as a function of the reaction energy on the clusters growth process. The blue dotted line indicates a linear relationship ($R^2 = 0.9$) of the solid-black points.

510 K in 10 K steps.

Experimentally, the prepared catalysts' metal dispersion varies depending on its composition and its preparation method. For example, a 12 wt% Ni/ Al_2O_3 catalyst used for hydrogenation reactions has a metal dispersion of around $150 \text{ m}^2 \text{ g}^{-1}$, [60] a 1–20 wt% Cu in $CuO/Al_2O_3-ZrO_2$ catalysts for the synthesis of biofuel 2-methyl furan has metal dispersion ranges between $180\text{--}536 \text{ m}^2 \text{ g}^{-1}$, [61] a 1 wt% Au- SiO_2 catalyst has been reported with a metal dispersion of $18 \text{ m}^2 \text{ g}^{-1}$, which is increased to $101 \text{ m}^2 \text{ g}^{-1}$ when alloyed with Pd. [62] We are considering here a model with Au dispersions significantly higher than typically achieved for heterogeneous catalysts, as the implemented bottom-up approach provides control at atomic-level. We defined the initial ($t = 0 \text{ s}$) coverage (θ) as the occupation of cells containing Au_X ($X = 1$ for ripening and 10 for digestion) to be 0.1, 0.5 and 0.9 monolayers (ML), giving 10% 50% and 90% of the maximum metal dispersion of $8608.44 \text{ m}^2 \text{ g}_{Au}^{-1}$. Notice that a monolayer is defined as one Au atom per slab area and, therefore, the maximum Au_{10} coverage is a tenth of the initial θ_1 in agreement with the reaction stoichiometry. The highest initial coverage of Au_{10} is 0.1 ML.

Fig. 6 illustrates the θ_{Au1} decrease as a function of increasing temperature due to its sintering, which initiates slightly above 100 K. After one minute at 150 K, Au_1 coalescence reached 0.26%, 2.26% and 12.18% of its respective initial coverage, i.e. 0.1, 0.5 and 0.9 ML. The steep slope observed between 180 and 240 K indicates that this process

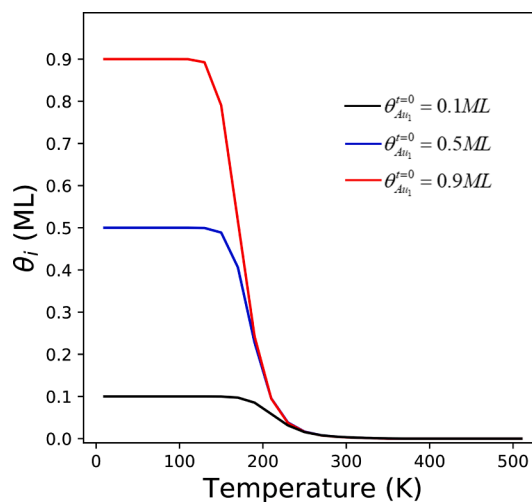


Fig. 6. Fractional occupation (θ) of Au_1 on $MgO(001)$ as a function of temperature after 60 s.

is happening very fast, especially at large coverages. At 370 K, the concentration of Au_1 is below 10^{-6} ML for any simulation. Fig. 7 illustrates further details on θ_{Au1} with respect to the temperature and time ($t < 0.01 \text{ s}$), where it is clear the accelerating effect of high temperatures, i.e. the descending slope, which perfectly fits with experimental observations on the increases of the atoms' mobility and the diffusion rates across the surface, see 3.1 single-atom migration mechanism. [63] At lower coverages, the sintering process is slower by the fact that individual atoms have less chance of meeting another atom.

The end-results of Au_1 coalescence is the formation of Au_{10} as can be observed in Figs. 8 and 9. In fact, most of Au_1 converts into Au_{10} after 1 s at 290 K. The remaining 4%, 0.9% and 0.5% of the initial Au atoms are in a different clusters' size than Au_{10} , respectively for the initial 0.1, 0.5 and 0.9 ML. Au_{10} coverage keeps increasing with time until reaching a plateau at a tenth of the initial Au_1 coverage, i.e. 0.01, 0.05 and 0.09. It is worth mentioning that, among the structures remaining, Au_4 is the most prominent, see Fig. 9, in agreement with its stability and activation energy to growth, see Table 2. Au_4 coverage grows very quickly, acting as Au sink, before leading to larger species. Notice that Au_{10} could increase further upon including the process in the simulation scheme, which implies the computationally demanding exploration of supported Au_m ($m > 10$) structures and transition states for a single atom coalescence.

3.4. Cluster digestion

To simulate the digestion process, i.e. forming smaller moieties from large clusters, the microkinetic experiment starts with Au_{10} on the same MgO surface with a 0.1 ML coverage. The presence of Au_{10} remains consistently high during the 60 s simulated, in agreement with the energy profiles, although the system's dynamic behaviour can be seen in Fig. 10. Au_{10} temporarily decreases at $\sim 160 \text{ K}$ leading to Au_9 and Au_8 as well as Au_1 and products of its coalescence. Fig. 11 shows the species with the most significant coverages derived from Au_{10} at 160 K and 1 s of the reaction time. The increase in the Au_{10} occupation at higher temperature is explained by the rise in energy allowing further movement to the atoms which remain for longer in the most stable conformation, i.e. Au_{10} .

The observed digestion of Au_{10} has significant implications in the design of supported Au nanostructures. Although they can be synthesized with minimal size dispersion, they present a dynamic size according to the conditions to which they are exposed, e.g. initial Au_{10} digests to Au_9 and Au_{11} . [64]

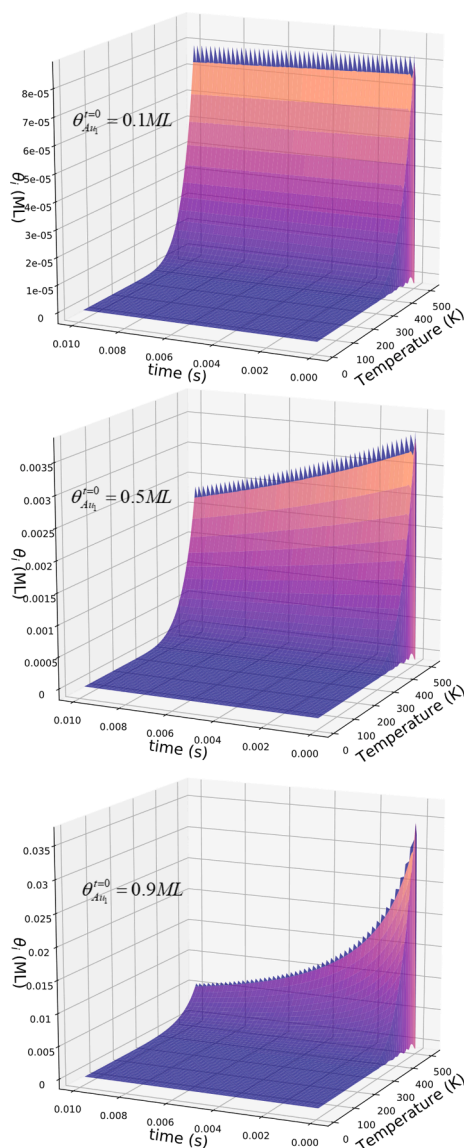


Fig. 7. Illustration of the Au_1 concentration as a function of the time and temperature at initial coverages (top) $\theta_{Au_1}^{t=0} = 0.1ML$, (middle) $\theta_{Au_1}^{t=0} = 0.5ML$, and (bottom) $\theta_{Au_1}^{t=0} = 0.9ML$.

4. Conclusion

We have combined DFT and microkinetics methods to unravel the Ostwald ripening and digestion of Au_n nanoparticles ($n \leq 10$ atoms) supported on $MgO(001)$. From the calculated adsorption, binding and cohesion energies and charge transfer analyses, we found that Au clusters' growth leads to the increasing importance of inter-metallic interactions compared to interactions between the metal cluster and the surface. Furthermore, although significant stability was found in the largest cluster, the energies present an odd-even trend caused by the spin magnetization of odd-numbered clusters and single atoms, and the activation barriers for an Au atom to coalescence are not larger than 1.05 eV. Beyond the odd-even effect of reaction energies, it appears to be a linear correlation between reaction and activation energies in the same fashion that there is for chemical reactions, i.e. Brønsted-Evans-Polanyi, which may have important implications in predicting ripening mechanisms.

The microkinetic simulations provided a bottom-up approach giving comparable results to macroscopic studies of nanoparticles coalescence. From the observations here reported, one can conclude that: (i) at low

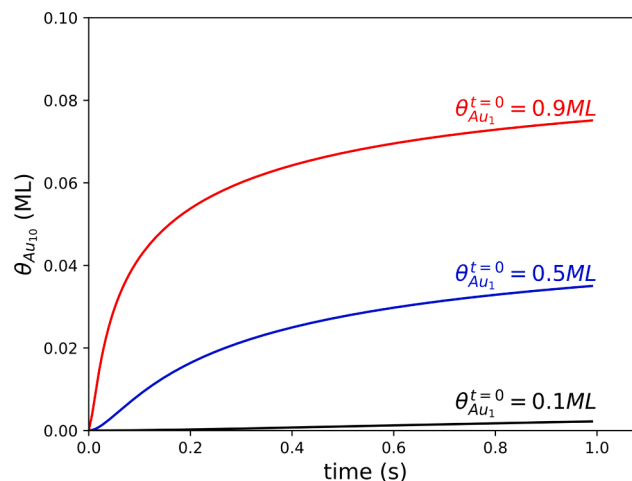


Fig. 8. Increasing Au_{10} coverage as a function of time for different initial Au_1 coverages at a temperature of 290 K.

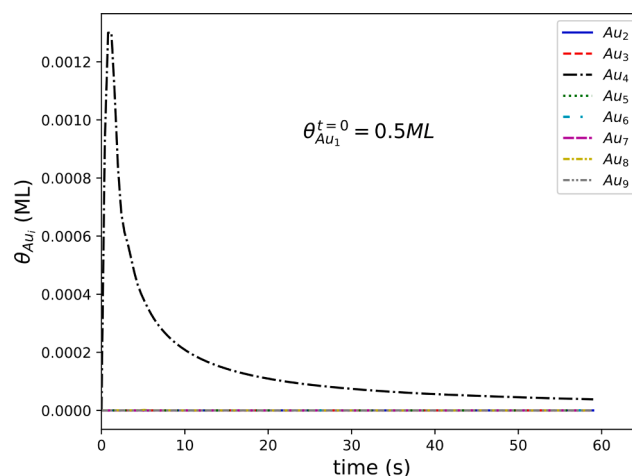


Fig. 9. Coverage of Au_i ($1 < i < 10$) clusters as a function of time at an initial $\theta_{Au_1} = 0.5 ML$ and a temperature of 290 K.

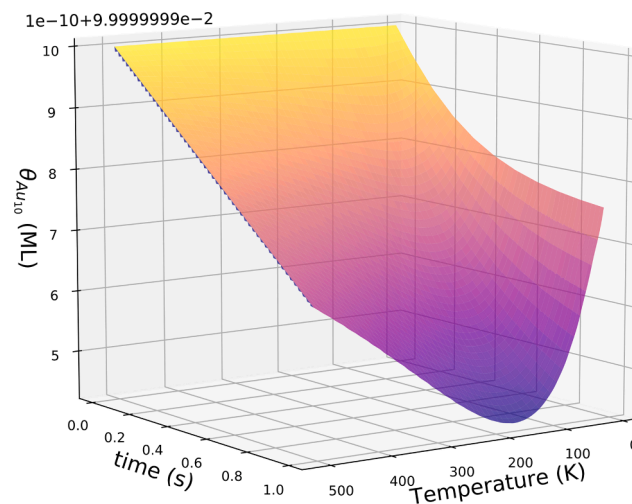


Fig. 10. Decrease in the Au_{10} occupation as a function of the reaction time and temperature for an initial Au_{10} coverage of 0.1 ML.

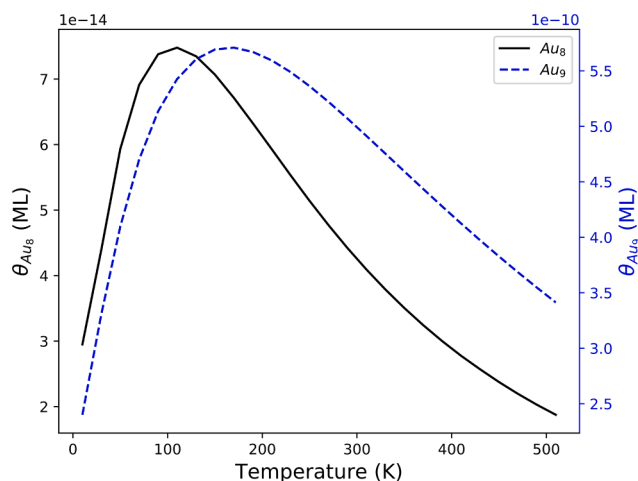


Fig. 11. Coverage of Au_8 and Au_9 derived from Au_{10} after being treated at 160 K for 1 s.

coverages, the smaller clusters will remain for longer on the surface than at high coverages as they are less likely to aggregate, (ii) at temperatures higher than 160 K, there is enough energy in the system for the atom to overcome the ripening barrier and diffuse across the pristine surface to interact with other species on the surface, (iii) large moieties, such as Au_{10} , also have a dynamic behaviour, easier to observe at relatively low temperatures, leading to size dispersion such as Au_8 and Au_9 , but also to larger clusters (not included in this report). Overall, we presented an innovative 'bottom-up' approach providing new insights on the behaviour of single atoms, clusters and nanoparticles and the diffusion and coalescence pathways with the rational of electronic structure calculations.

Declaration of Competing Interest

The authors declare that they have no known competing financial interests or personal relationships that could have appeared to influence the work reported in this paper.

Acknowledgements

We thank the EPSRC for the support through the EP/P005845/1 grant. Via our membership of the UK's HEC Materials Chemistry Consortium, which is funded by EPSRC (EP/L000202), this work used the UK Materials and Molecular Modelling Hub for computational resources, MMM Hub, which is partially funded by EPSRC (EP/P020194). We also acknowledge computing time on the facilities of Supercomputing Wales and the Advanced Research Computing @ Cardiff (ARCCA) at Cardiff University. All data created during this research are openly available from the University of Cardiff Research Portal orca websites: <http://doi.org/10.17035/d.2021.0137591611>.

Appendix A. Supplementary material

Supplementary data to this article can be found online at <https://doi.org/10.1016/j.apsusc.2021.151317>.

References

- Tao, F. (Feng), Schneider, W. F. & Kamat, P. V. *Heterogeneous Catalysis at Nanoscale for Energy Applications*. (Wiley, 2015).
- S. Mostafa, et al., Shape-Dependent Catalytic Properties of Pt Nanoparticles, *J. Am. Chem. Soc.* 132 (2010) 15714–15719.
- Yudan Wang, Zhichao Tao, Baoshan Wu, Huimin Chen, Jian Xu, Yong Yang, Yongwang Li, Shape-controlled synthesis of Pt particles and their catalytic performances in the n-hexadecane hydroconversion, *Catal. Today* 259 (2016) 331–339.
- R. van den Berg, et al., Structure sensitivity of Cu and CuZn catalysts relevant to industrial methanol synthesis, *Nat. Commun.* 7 (2016) 20457–20465.
- Masatake Haruta, Size-and support-dependency in the catalysis of gold, *Catal. Today* 36 (1) (1997) 153–166.
- Q. Fu, A. Weber, M. Flytzani-Stephanopoulos, Nanostructured Au–CeO₂ catalysts for low-temperature water–gas shift, *Catal. Letters* 77 (2001).
- C. Mebrahtu, F. Krebs, S. Abate, G. Centi, R. Palkovits, CO₂ Methanation: Principles and Challenges, *Stud. Surf. Sci. Catal.* 178 (2019) 85–103.
- Calvin H Bartholomew, Mechanisms of catalyst deactivation, *Appl. Catal. A Gen.* 212 (1–2) (2001) 17–60.
- R. Ouyang, J.-X. Liu, W.-X. Li, Atomistic Theory of Ostwald Ripening and Disintegration of Supported Metal Particles under Reaction Conditions, *J. Am. Chem. Soc.* 135 (2013) 1760–1771.
- L. Ratke, P.W. Voorhees, *Growth and Coarsening: Ostwald Ripening in Material Processing*, Springer, Berlin Heidelberg, 2002.
- P. Wynblatt, N.A. Gjostein, Particle growth in model supported metal catalysts—I, Theory, *Acta Metall.* 24 (1976) 1165–1174.
- A. Baldan, Review Progress in Ostwald ripening theories and their applications to nickel-base superalloys Part I: Ostwald ripening theories, *J. Mater. Sci.* 37 (2002) 2171–2202.
- C.T. Campbell, et al., The Effect of Size-Dependent Nanoparticle Energetics on Catalyst Sintering, *Science* (80-) 298 (2002) 811–814.
- Charles T. Campbell, The Energetics of Supported Metal Nanoparticles: Relationships to Sintering Rates and Catalytic Activity, *Acc. Chem. Res.* 46 (8) (2013) 1712–1719.
- T.W. Hansen, A.T. DeLaRiva, S.R. Challa, A.K. Datye, Sintering of Catalytic Nanoparticles: Particle Migration or Ostwald Ripening? *Acc. Chem. Res.* 46 (2013) 1720–1730.
- V. Elofsson, *Nanoscale structure forming processes*, (Linköping University Electronic Press, 2016).
- Ostwald ripening. in *IUPAC Compendium of Chemical Terminology* (IUPAC, 2008). doi:10.1351/goldbook.o04348.
- Bartholomew, C. H., Fuentes, G. A. (Gustavo A. . & International Symposium on Catalyst Deactivation (7th : 1997 : Cancún, M. Catalyst deactivation 1997 : proceedings of the international symposium, Cancun, Mexico, October 5-8, 1997. (Elsevier, 1997).
- Masatake Haruta, Gold as a novel catalyst in the 21st century: Preparation, working mechanism and applications, *Gold Bull.* 37 (1-2) (2004) 27–36.
- G HUTCHINGS, Vapor phase hydrochlorination of acetylene: Correlation of catalytic activity of supported metal chloride catalysts, *J. Catal.* 96 (1) (1985) 292–295.
- Z. Wang, C. Xu, H. Wang, A Facile Preparation of Highly Active Au/MgO Catalysts for Aerobic Oxidation of Benzyl Alcohol, *Catal. Letters* 144 (2014) 1919–1929.
- M.D. Hughes, et al., Tunable gold catalysts for selective hydrocarbon oxidation under mild conditions. 437 (2005) 1132–1135.
- N.M. Julkapli, S. Bagheri, Magnesium oxide as a heterogeneous catalyst support, *Rev. Inorg. Chem.* 36 (2016) 1–41.
- Ivona Tomska-Foralewska, Michał Zieliński, Mariusz Pietrowski, Wiesław Przyszajko, Maria Wojciechowska, Iridium supported on MgF₂–MgO as catalyst for CO oxidation, *Catal. Today* 176 (1) (2011) 263–266.
- Mingzhou Wu, Yu Fu, Wangcheng Zhan, Yanglong Guo, Yun Guo, Yunsong Wang, Guanzhong Lu, Catalytic Performance of MgO-Supported Co Catalyst for the Liquid Phase Oxidation of Cyclohexane with Molecular Oxygen, *Catalysts* 7 (5) (2017) 155, <https://doi.org/10.3390/catal7050155>.
- Bajdich, M., Nørskov, J. K. & Vojvodica, A. Surface Energetics of Alkaline-Earth Metal Oxides: Trends in Stability and Adsorption of Small Molecules. (2015).
- Y. Cho, et al., First-principles study on secondary electron emission of MgO surface, *J. Appl. Phys.* 101 (2007), 083710.
- P. Wu, G. Cao, F. Tang, M. Huang, Electronic and magnetic properties of transition metal doped MgO sheet: A density-functional study, *Comput. Mater. Sci.* 86 (2014) 180–185.
- K.J. Chang, M.L. Cohen, High-pressure behavior of MgO: Structural and electronic properties, *Phys. Rev. B* 30 (1984) 4774–4781.
- Zhao Jian-Zhou, Lu. Lai-Yu, Y.-L. Xiang-Rong Chen, First-principles calculations for elastic properties of the rocksalt structure MgO, *Phys. B Condens. Matter* 387 (2007) 245–249.
- G.W. Watson, E.T. Kelsey, N.H. de Leeuw, D.J. Harris, S.C. Parker, Atomistic simulation of dislocations, surfaces and interfaces in MgO, *J. Chem. Soc. Faraday Trans.* 92 (1996) 433.
- Claude R. Henry, Surface studies of supported model catalysts, *Surf. Sci. Rep.* 31 (7–8) (1998) 231–325.
- J.K. Nørskov, T. Bligaard, J. Rossmeisl, C.H. Christensen, Towards the computational design of solid catalysts, *Nature chemistry* 1 (1) (2009) 37–46.
- N. Lopez, et al., On the origin of the catalytic activity of gold nanoparticles for low-temperature CO oxidation. 223 (2004) 232–235.
- M. Cargnello, et al., Control of Metal Nanocrystal Size Reveals Metal-Support Interface Role for Ceria Catalysts, *Science* (80-) 341 (2013) 771–773.
- M.J. Walsh, et al., On the Structural Origin of the Catalytic Properties of Inherently Strained Ultrasmall Decahedral Gold Nanoparticles, *Nano Lett.* 12 (2012) 2027–2031.
- K. Blick, et al., Methane oxidation using Au/MgO catalysts, *Catal. Letters* 50 (1998) 211–218.
- G. Kresse, J. Hafner, Ab initio molecular dynamics for liquid metals, *Phys. Rev. B* 47 (1) (1993) 558–561.

- [39] G. Kresse, J. Furthmüller, Efficient iterative schemes for ab initio total-energy calculations using a plane-wave basis set, *Phys. Rev. B* 54 (16) (1996) 11169–11186.
- [40] G. Kresse, D. Joubert, From ultrasoft pseudopotentials to the projector augmented-wave method, *Phys. Rev. B* 59 (3) (1999) 1758–1775.
- [41] J.P. Perdew, K. Burke, M. Ernzerhof, Generalized Gradient Approximation Made Simple, *Phys. Rev. Lett.* 77 (1996) 3865–3868.
- [42] P.E. Blöchl, Projector augmented-wave method, *Phys. Rev. B* 50 (24) (1994) 17953–17979.
- [43] S. Grimme, J. Antony, S. Ehrlich, H. Krieg, A consistent and accurate ab initio parametrization of density functional dispersion correction (DFT-D) for the 94 elements H-Pu, *J. Chem. Phys.* 132 (2010), 154104.
- [44] J. Engel, S. Francis, A. Roldan, The influence of support materials on the structural and electronic properties of gold nanoparticles – a DFT study, *Phys. Chem. Chem. Phys.* 21 (2019) 19011–19025.
- [45] X. Lu, J. Zhang, W.-K. Chen, A. Roldan, Kinetic and mechanistic analysis of NH₃ decomposition on Ru(0001), Ru(111) and Ir(111) surfaces, *Nanoscale Adv.* 3 (2021) 1624–1632.
- [46] Petr Ptáček, František Šoukal, Tomáš Opravil, in: *Introducing the Effective Mass of Activated Complex and the Discussion on the Wave Function of this Instanton*, InTech, 2018, <https://doi.org/10.5772/intechopen.78705>.
- [47] A. Roldán, G. Novell, J.M. Ricart, F. Illas, Theoretical simulation of temperature programmed desorption of molecular oxygen on isolated Au nanoparticles from density functional calculations and microkinetics model, *J. Phys. Chem. C* 114 (2010) 5101–5106.
- [48] K. Agrawal, A. Roldan, N. Kishore, A.J. Logsdail, Dehydrogenation and dehydration of formic acid over orthorhombic molybdenum carbide, *Catal. Today* (2021), <https://doi.org/10.1016/j.cattod.2021.04.011>.
- [49] S.S. Tafreshi, A. Roldan, N.H. de Leeuw, Density functional theory calculations of the hydrazine decomposition mechanism on the planar and stepped Cu(111) surfaces, *Phys. Chem. Chem. Phys.* 17 (2015) 21533–21546.
- [50] Ali Hussain Motagamwala, James A. Dumesic, Microkinetic Modeling: A Tool for Rational Catalyst Design, *Chem. Rev.* 121 (2) (2021) 1049–1076, <https://doi.org/10.1021/acs.chemrev.0c00394>.
- [51] H. Eyring, M. Polanyi, Concerning simple gas reactions. *ZEITSCHRIFT FÜR Phys. CHEMIE-ABTEILUNG B-CHEMIE DER Elem, AUFBAU DER Mater.* 12 (1931) 279–311.
- [52] Y. Peng, et al., Two-step nucleation mechanism in solid–solid phase transitions, *Nat. Mater.* 14 (2015) 101–108.
- [53] Riccardo Ferrando, Alessandro Fortunelli, Diffusion of adatoms and small clusters on magnesium oxide surfaces, *J. Phys. Condens. Matter* 21 (26) (2009) 264001, <https://doi.org/10.1088/0953-8984/21/26/264001>.
- [54] M. Yulikov, M. Sterrer, T. Risse, H.-J. Freund, Gold atoms and clusters on MgO (100) films; an EPR and IRAS study, *Surf. Sci.* 603 (2009) 1622–1628.
- [55] Einstein, A. & Fürth, R. (Reinhold). *Investigations on the theory of Brownian movement.* (Dover Publications, 1956).
- [56] H. Yildirim, A. Kara, S. Durukanoglu, T.S. Rahman, Calculated pre-exponential factors and energetics for adatom hopping on terraces and steps of Cu(100) and Cu (110), *Surf. Sci.* 600 (2006) 484–492.
- [57] Konstantina Damianos, Riccardo Ferrando, Determination of the structures of small gold clusters on stepped magnesia by density functional calculations, *Nanoscale* 4 (4) (2012) 1101–1108.
- [58] S. Bucak, D. Rende, *Colloid and surface chemistry : a laboratory guide for exploration of the Nano world*, Cambridge University Press, 2014.
- [59] S. Campisi, et al., DFT-Assisted Spectroscopic Studies on the Coordination of Small Ligands to Palladium: From Isolated Ions to Nanoparticles, *J. Phys. Chem. C* 124 (2020) 4781–4790.
- [60] R. Geyer, et al., Methods for Determining the Metal Crystallite Size of Ni Supported Catalysts, *Chemie Ing. Tech.* 84 (2012) 160–164.
- [61] G.V. Sagar, P.V.R. Rao, C.S. Srikanth, K.V. Chary, Dispersion and reactivity of copper catalysts supported on Al₂O₃–ZrO₂, *The J of Phys Chem B* 110 (28) (2006) 13881–13888.
- [62] H. Bönemann, et al., An SiO₂-Embedded Nanoscopic Pd/Au Alloy Colloid, *Eur. J. Inorg. Chem.* 2000 (2000) 819–822.
- [63] Randall M. German, in: *Sintering: from Empirical Observations to Scientific Principles*, Elsevier, 2014, pp. 183–226, <https://doi.org/10.1016/B978-0-12-401682-8.00007-0>.
- [64] M. Sankar, et al., Role of the Support in Gold-Containing Nanoparticles as Heterogeneous Catalysts, *Chem. Rev.* 120 (2020) 3890–3938.